© Universiti Tun Hussein Onn Malaysia Publisher's Office

IJIE

http://penerbit.uthm.edu.my/ojs/index.php/ijie
ISSN : 2229-838X e-ISSN : 2600-7916

The International Journal of Integrated Engineering

Influence of Rotor Pole Number on the Output of Double Stator Flux-Switching Machine

Chukwuemeka C. Awah[1*], Ifeanyi K. Nnabuenyi[2], Cyril A. Amaghionyeodiwe[3], Stephen E. Oti[4], Ogbonnaya Obasi[1]

[1]Department of Electrical and Electronic Engineering,
Michael Okpara University of Agriculture, Umudike, NIGERIA

[2]Instrument QA/QC Arco M&E, NLNG Sub Contractor, Bonny, Rivers State, NIGERIA

[3]Department of Mechanical Engineering,
Michael Okpara University of Agriculture, Umudike, NIGERIA

[4]Department of Electrical Engineering,
University of Nigeria, Nsukka, NIGERIA

*Corresponding Author

DOI: https://doi.org/10.30880/ijie.2023.15.07.024
Received 13 September 2023; Accepted 03 December 2023; Available online 31 December 2023

Abstract: Influence of rotor pole numbers on the output performance of a double stator flux-switching permanent magnet machine is investigated and compared in this study. A description of the analyzed machine is first given. Maxwell-2D time-stepping finite element analysis is adopted in estimating the results. The no-load and load characteristics of the investigated machine is considered and quantitatively compared amongst four different rotor pole configurations. The compared machine categories are designated as: 6S/10P, 6S/11P, 6S/13P and 6S/14P, where P stands for rotor pole and S stands for stator slot. It is revealed that the compared 6S/11P machine topology has a lot of good qualities amongst all the compared machine types, since it exhibits the largest electromotive force (EMF), power, torque and greatest overload sustainability feature, etc. Though, the 6S/14P has excellent flux-weakening capability. Moreover, the 6S/13P machine configuration would produce the largest torque if all the compared machines are equipped with same amount of permanent magnet volume/material. The compared machine topologies have reasonably good anti-demagnetization potentials; particularly, the 6S/13P topology.

Keywords: Electromotive force, flux linkage, pole numbers, power and torque

1. Introduction

Permanent magnet machines of high torque and power densities are usually preferred in most industrial and domestic drive applications. Most often the double stator permanent magnet machines (DSPMM) are ideal for such drive applications, owing to its excellent output performances compared to equivalent single stator single rotor machines [1]. Thus, a double stator permanent magnet machine having reasonably high output torque is investigated in this research, with more emphasis on the influence of rotor pole number on its resulting performance(s). The studies in [1] show that practical combinations of rotor pole number and stator slot number would have significant influence on the overall output performance of a given electrical machine; ranging from the produced flux density, generated electromotive force to resulting torque features. Hence, optimal combinations of rotor pole and stator slot numbers are essential in the design and analysis of electric machines, for improved overall output. It is worth mentioning that the

*Corresponding author: author@uthm.edu.my
2023 UTHM Publisher. All rights reserved.

compared machine types in this current study are high-torque low-speed machines and are suitable for direct-drive applications.

Similarly, effect of pole ratios on the output performance of two different permanent magnet machine topologies is compared in [2]. The investigation shows that the effect of leakage flux would increase in a given flux-modulation electric machine, when its pole ratio value increases, irrespective of its flux-concentration advantage that enables high output torque production; this drawback may indirectly affect the machine's cost-effectiveness. It is worth noting that the magnets of the compared machines in this present study are arranged in spoke-like style, and they utilize the flux-concentration technique, for improved output torque. Note that the compared topologies in this current investigation operate as both flux-modulation and flux-switching permanent magnet machines. The ability of flux-switching permanent magnet (FSPM) machines to effectively utilize flux-concentration skill in its flux density and torque production is highlighted in [3]. High flux-leakage effect of machines that have high number of rotor poles, as well as the significant impact of rotor pole number on the machine's overall output performance is reconfirmed in [4].

In [5], deployment of flux-focusing technique is proved to have significant positive effect on the electromagnetic performance of a given electrical machine, coupled to the inherent influence of stator and rotor pole number combination. Electric machines that are furnished with very small number of rotor pole may also experience high flux-leakage, as noted in [6]. Moreover, magnitude of self- and mutual-inductance and its consequent fault-tolerance ability of a given permanent magnet machine would be determined by its slot number and rotor pole number permutations. Additionally, it is proved in [6] that the generated electromotive force (EMF) and resulting output torque of the machine, as well as the machine's winding factor would be dependent upon its stator and rotor pole number arrangements; besides its influence on the machine's ability to withstand electromagnetic saturation effects.

Further, electric and magnetic loadings of permanent magnet machines which are functions of a machines' magnetomotive force and winding factors depending on the machine's pole and stator pole number feasibility, would considerably influence the resulting electromagnetic performance of the machine, as demonstrated in [7]. These pole number arrangements would also determine the amount of undesirable machine qualities such as no-load torque and torque pulsations, etc. Nevertheless, a machine's overall diameter is also a great determinant of the resulting output performance.

Basically, influence of rotor pole number on the output performance of a given flux-switching permanent magnet machine having double stator structure is investigated and quantitatively compared in this present study. The study is presented in five (5) sections, ranging from introduction, machine description, no-load and load characteristics to conclusion.

2. Machine Description and Methodology

Three-dimensional diagram of the analyzed machine is displayed in Fig. 1(a). Finite element analysis (FEA) method is deployed in the whole computations through the use of MAXWELL-ANSYS software. It is important to note that the investigated double stator machine has three-phase alternating current (AC) windings in both the inner and outer stators; however, these windings are joined together in series for enhanced output performance. Overall size of the investigated machine is 90 mm with an axial stack length of 25 mm. The active air gap size is 0.5 mm. The core sections are made of silicon steel material. The magnets are made of neodymium-iron-boron material. Meanwhile, the total number of turns per phase is 72. The studied machine types are: I. 6S/10P i.e. 6 slots and 10 poles machine type. II. 6S/11P i.e. 6 slots and 11 poles machine type. III. 6S/13P i.e. 6 slots and 13 poles machine type. IV. 6S/14P i.e. 6 slots and 14 poles machine type, respectively. Relationship between the stator slot and rotor pole numbers of the compared machine types is given in Eq. 1 and Eq. 2, as provided in [8] and [9]. Simulation setup on two-dimensional finite element platform of the analyzed 6S/11P machine type is displayed in Fig. 1 (b). The various sections of Fig. 1 (b) include:

(I) Project manager section i.e. an environment for model design and solution setup. It is worth noting that coil excitations, core loss and eddy current settings, as well as the mesh distributions and the consequent magnetic field overlays of the model is executed in the Project manager section.

(II) Material sheet section i.e. for assigning different materials/properties such magnet material, stator and rotor core/steel materials, air and vacuum etc., to the relevant parts of the machine.

(III) Design properties i.e. for assigning variables names with its relevant values and units. This section also takes care of model optimetrics and multiple scanning operations, etc.

(IV) Coordinate systems and planes, etc. Note that a global coordinate system is adopted in this investigation.

No-load characteristics of the investigated model are achieved by inputting zero (0) currents to three-phase windings of the machine, located in the excitation window. The electrical frequency (f_e) of the model is provided in Eq. 3. On simulating the model over an electrical revolution, the phase flux linkages, no load torque and induced electromotive force are automatically generated by the adopted computer software and archived as an excel file. The file is exported and saved as a ".csv" file, for further graph plotting. Similarly, load characteristics are initiated by magnetizing the three-phase windings with phase sinusoidal currents spaced at 120^o electrical degrees apart from each other. The magnitude of the applied rated current is 15 A. Basically, on exciting the stator phase windings with phase

currents, three-phase flux linkage is produced which will then generate induced electromotive force (EMF) over time. The EMF is predicted as a rate of change of flux over a given time. This action will cause the rotor to move in the direction of stator magnetic fields, for possible torque production. It is important to note that each magnet must be placed adjacent to each other with opposite polarity or charge sign, in order to produce the needed torque. Overall, machine output performances such as induced electromotive force, flux linkage, torque, force, losses and efficiency of the analyzed machine types are investigated in this article, with special reference made to influence of pole number on the machine's output characteristics.

$$P_r = 2P_s \pm 1 \quad (1)$$

$$P_r = 2P_s \pm 2 \quad (2)$$

where: P_r is number of rotor poles, P_s is number of stator slots.

$$f_e = \frac{P_r N}{60} \quad (3)$$

where: N is the rotor speed in r/min [9].

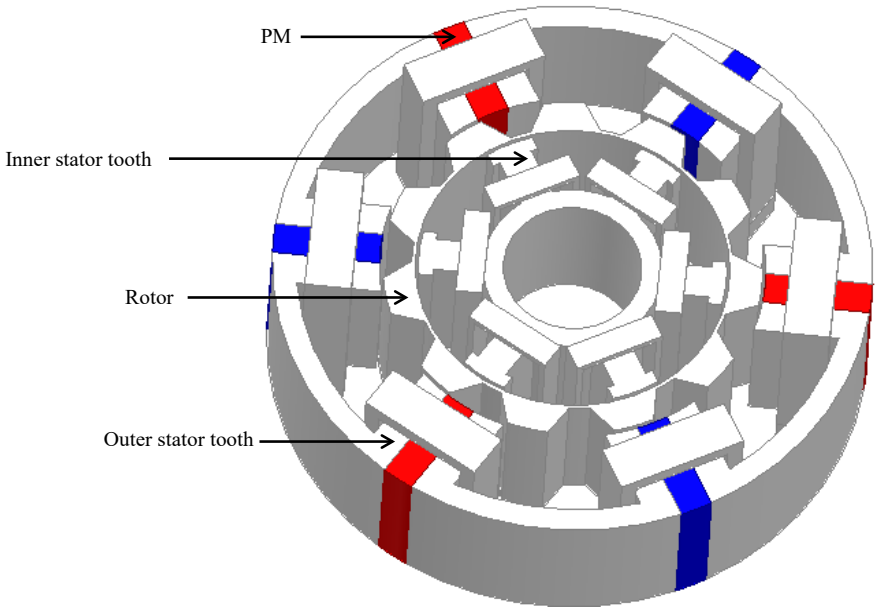

(a) 3D structure of 6S/11P

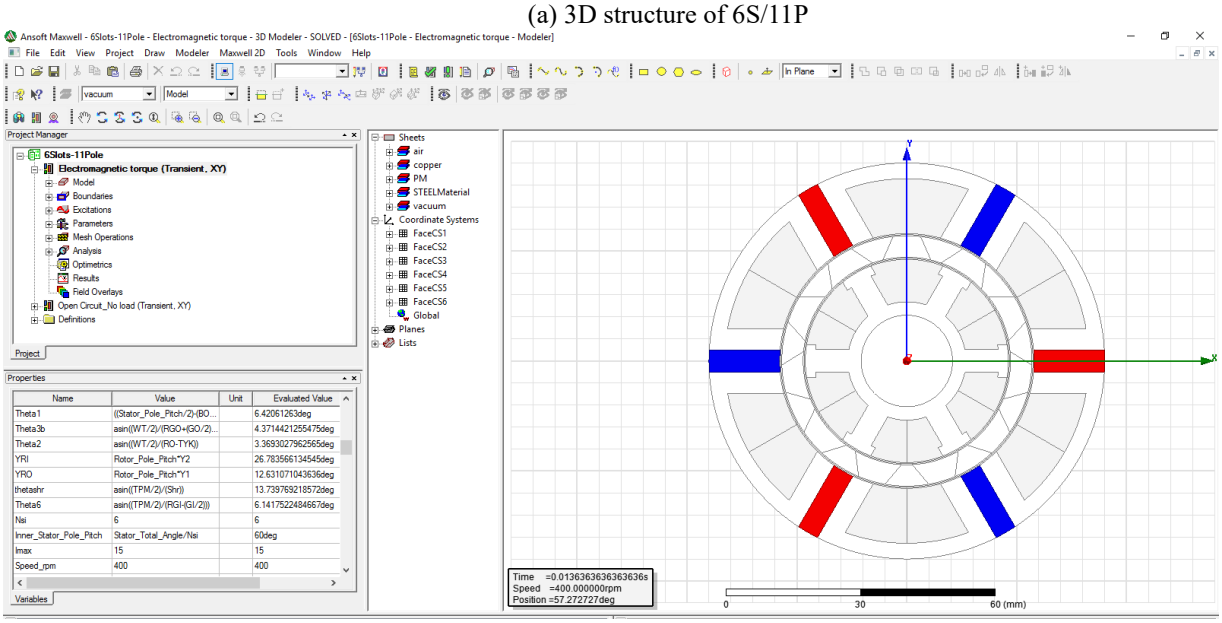

(b) Extracted 2D-FEA simulation platform of 6S/11P

Fig. 1 - 2D-FEA and 3D-FEA structures of the analyzed machine having 11 rotor poles

3. No-Load Characteristics

The magnetic flux density contours of the compared machine types on open-circuit (no-load) condition are shown in Fig. 2. It is observed that the iron cores would have highest susceptibility to saturation impact, particularly around the air gap periphery. The compared machine parameters are listed in Table 1. The weight of the machine parts are measured directly from 3D-FEA structures of the compared machine. The simulation is conducted at a rated speed of 400 r/min and rated load current of 15 A. The total number of turns per phase is 72; thus, 36 turns in each of the two coils that make up a Phase. Magnetic remanence of the implemented magnet material (N35SH) is 1.2 Tesla with a permeability of 1.05. Default ambient temperature setting of the implemented software is 20 ºC.

Similarly, the generated flux linkage in Phase A of the compared machine types is depicted in Fig. 3; the phase flux linkage of the 6S/11P machine type is over 56 % larger than the least performing machine type, i.e. the 6S/14P. More so, noticeable harmonic contents are observed in the machine types having 6S/14P and 6S/10P, as could be deduced from Fig. 3(b); these harmonics are undesirable for smooth operation and control of a given electric machine. It is also observed that the 6S/11P and 6S/13P machine topologies have symmetric and complete sinusoidal flux linkage waveforms. A symmetrical and sinusoidal flux linkage and EMF waveforms would be obtained from a given permanent magnet machine by implementing appropriate combination of rotor pole and stator teeth numbers, as highlighted in [9]. It is worth noting flux linkage of any given electrical machine is directly related to its corresponding EMF, because EMF is the rate of change of flux over a given time. Hence, the flux linkage harmonic characteristics are invariably related to that of its EMF equivalents. In order to obtain a symmetrical EMF waveform in the analyzed machine; then, the ratio of its rotor pole number to stator tooth number must be equivalent to the ratio of an odd numerator integer to an even denominator integer, as stated in [9].

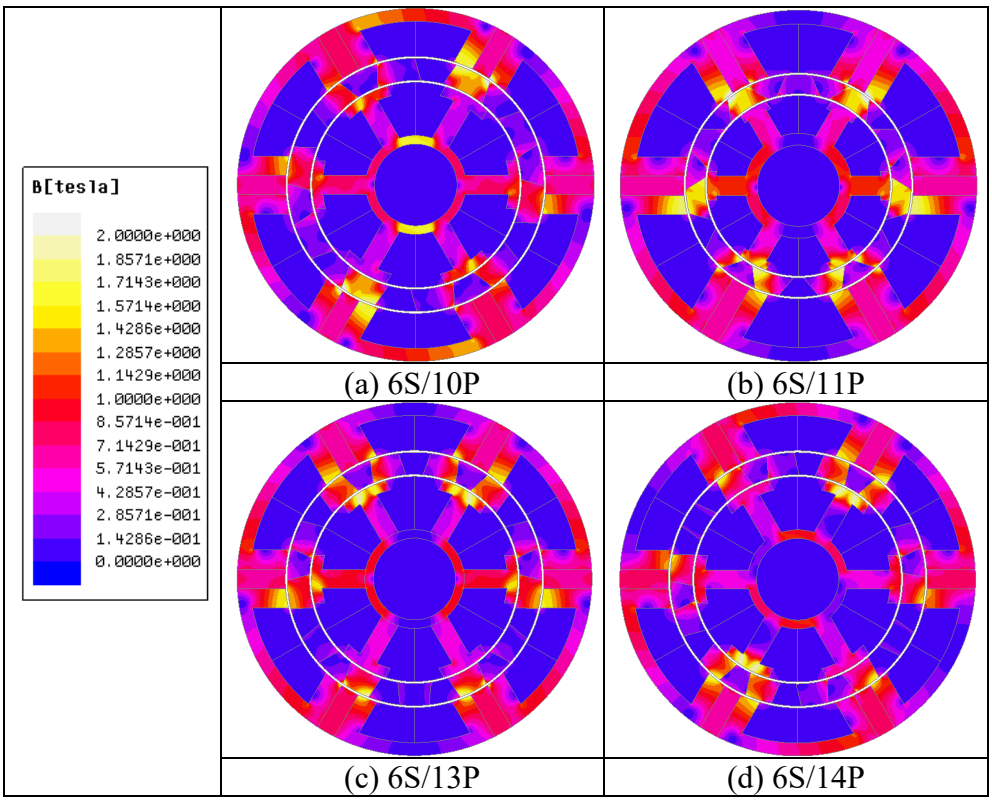

Fig. 2 - Flux-density, 2D FEA no-load

Table 1 - Compared machine parameters

Machine parameter	6S/10P	6S/11P	6S/13P	6S/14P
Rotor weight (kg)	0.0349	0.0276	0.0349	0.0349
Rotor weight (kg)	0.0349	0.0276	0.0349	0.0349
Outer rotor diameter (mm)	64.5328	56.8944	64.5328	65.3288
Stator slot number	6			
Outer stator radius (mm)	45			
Magnet permeability	1.05			
Machine base speed (r/min)	400			

Rated current (A)	15
Grade of magnet	N35SH
Stator and rotor core material	Silicon steel
Conductor material	Copper
Material conductivity (S/m)	2.22 x 10^6
Ambient temperature (°C)	20
Magnetic remanence (Tesla)	1.2
Winding factor	0.6
Number of turns in the series coil	36

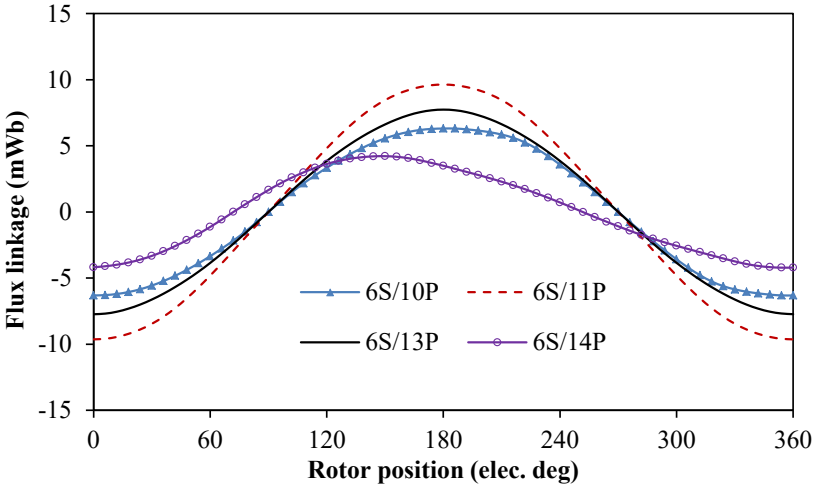

(a) Phase flux linkage

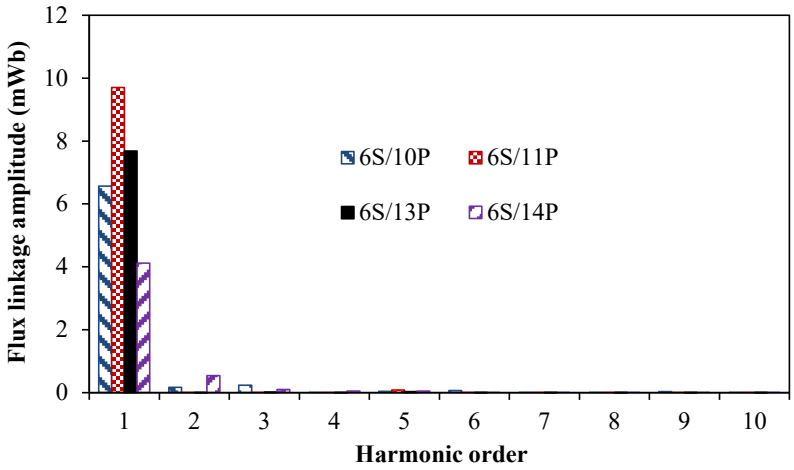

(b) FFT amplitude

Fig. 3 - Comparison of flux linkage at 400 r/min

Electromotive force (EMF) waveforms and its resulting fast Fourier transform (FFT) harmonic values are presented in Fig. 4 (a) and (b). A direct FEA extraction of the EMF and flux linkage waveforms is displayed in Fig 4 (c). The obtained EMF waveform is both symmetrical and sinusoidal in 6S/13P machine topology; though the 6S/11P EMF waveform is also symmetrical about the rotor positions, however, with a flattened peak. Sinusoidal nature of a given machine's EMF waveform is synonymous to its control amenability. Thus, the 6S/13P machine type would exhibit the most exciting electric machine control flexibility, followed by its 6S/11P equivalent. Nevertheless, largest EMF magnitude is produced by the 6S/11P, while the least EMF value is obtained by 6S/14P machine type. It is worth noting that 6S/10P and 6S/14P machine categories have both asymmetric and non-sinusoidal EMF waveforms, and these are flaws/drawbacks in control of electric machines. These undesirable machine qualities may lead to high torque ripple, cogging torque, total harmonic distortion effects, unbalanced magnetic force and may consequently generate noise and vibrations in the system, as provided in [10], [11] and [12]. It is important to note that undesirable qualities of any given machine could negatively affect its electromagnetic torque and efficiency. Induced coil EMFs and its corresponding harmonic content mathematical expressions are provided in Eqs. 4–6, as presented in

[13], of typical flux-switching permanent magnet machine (FSPMM), to which the investigated machine in this present study belongs.

$$e_a = E_1 \sin(\omega t) + \sum_{n=2}^{\infty} E_n \sin(n\omega t + \varphi_n) \quad (4)$$

$$e_b = E_1 \sin(\omega t + 2\pi/3) + \sum_{n=2}^{\infty} E_n \sin[n(\omega t + 2\pi/3) + \varphi_n] \quad (5)$$

$$e_c = E_1 \sin(\omega t - 2\pi/3) + \sum_{n=2}^{\infty} E_n \sin[n(\omega t - 2\pi/3) + \varphi_n] \quad (6)$$

where: e_a, e_b and e_c is the EMF in each coil of the phases, ω is electrical rotor speed, φ_n is n-order harmonic angle relative to the fundamental phase, E_1 and E_n is amplitude of the fundamental and the nth order harmonic EMF, respectively [13]. Note that the resultant nth order harmonic of phase EMF is obtained as an algebraic sum of its individual coil EMFs [14].

Additionally, harmonic components of a typical FSPMM are dependent upon its coil pitch coefficients. Mathematical expression of coil pitch coefficient (k_c) of an FSPMM is stated in Eq. 7, as provided in [9].

$$k_c = \cos\left(\pi n\left(\frac{P_r}{P_s} - 1\right)\right) \quad (7)$$

where: n is n^{th} order harmonic.

For example, in determining the coil pitch coefficient of the third (3rd) in the compared machine types, the calculations are detailed as follows:

I. 6S/10P

$$k_c = \cos\left(\pi \times 3\left(\frac{10}{6} - 1\right)\right) = 1 \quad (8)$$

II. 6S/11P

$$k_c = \cos\left(\pi \times 3\left(\frac{11}{6} - 1\right)\right) = 0 \quad (9)$$

III. 6S/13P

$$k_c = \cos\left(\pi \times 3\left(\frac{13}{6} - 1\right)\right) = 0 \quad (10)$$

IV. 6S/14P

$$k_c = \cos\left(\pi \times 3\left(\frac{14}{6} - 1\right)\right) = 1 \quad (11)$$

From Eqs. 8–11, coil pitch coefficient (k_c) is equal to one (1) in 6S/10P and 6S/14P machine configurations; thus, it is noticeable in the 3rd harmonic order of induced voltage, as confirmed in Fig. 4 (b). Similarly, 6S/11P and 6S/13P machine types have zero (0) k_c value; hence, it is not manifested in the 3rd harmonic order of the induced voltage shown in Fig. 4(b). FEA extracted Phase A flux linkage and EMF waveforms are depicted in Fig. 4(c). An electrical machine with a high amount of 3rd harmonic EMF component would invariably have a high value of torque ripple [15]; this assertion is in agreement with the obtained torque ripple results of Fig. 8(a).

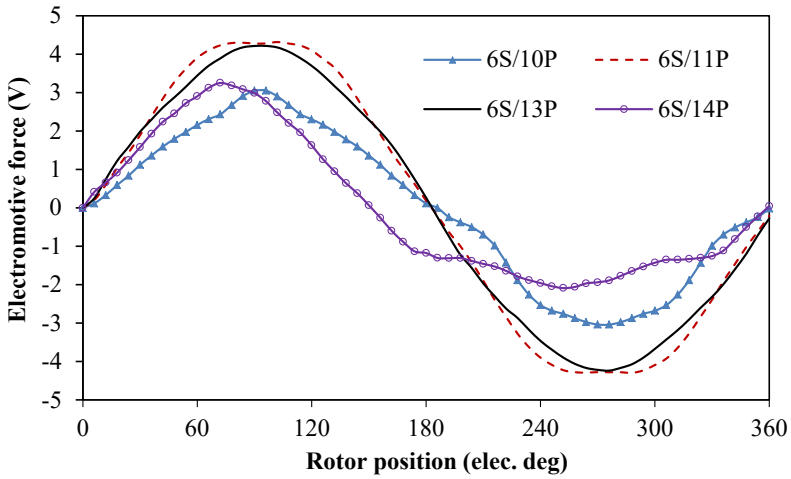

(a) Phase electromotive force

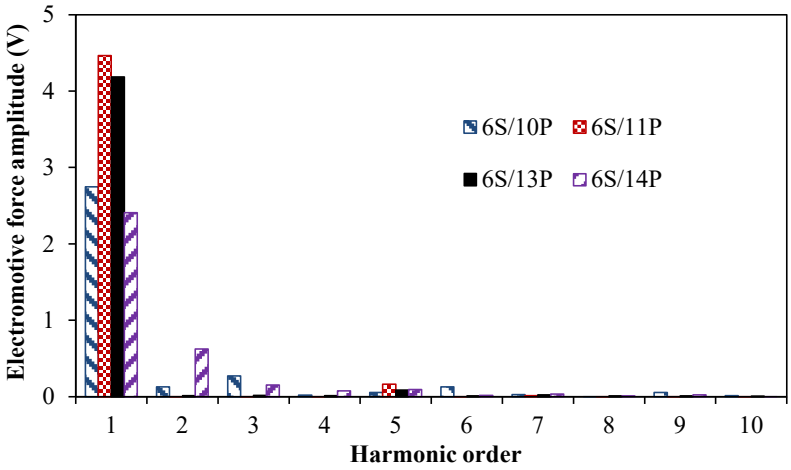

(b) FFT amplitude

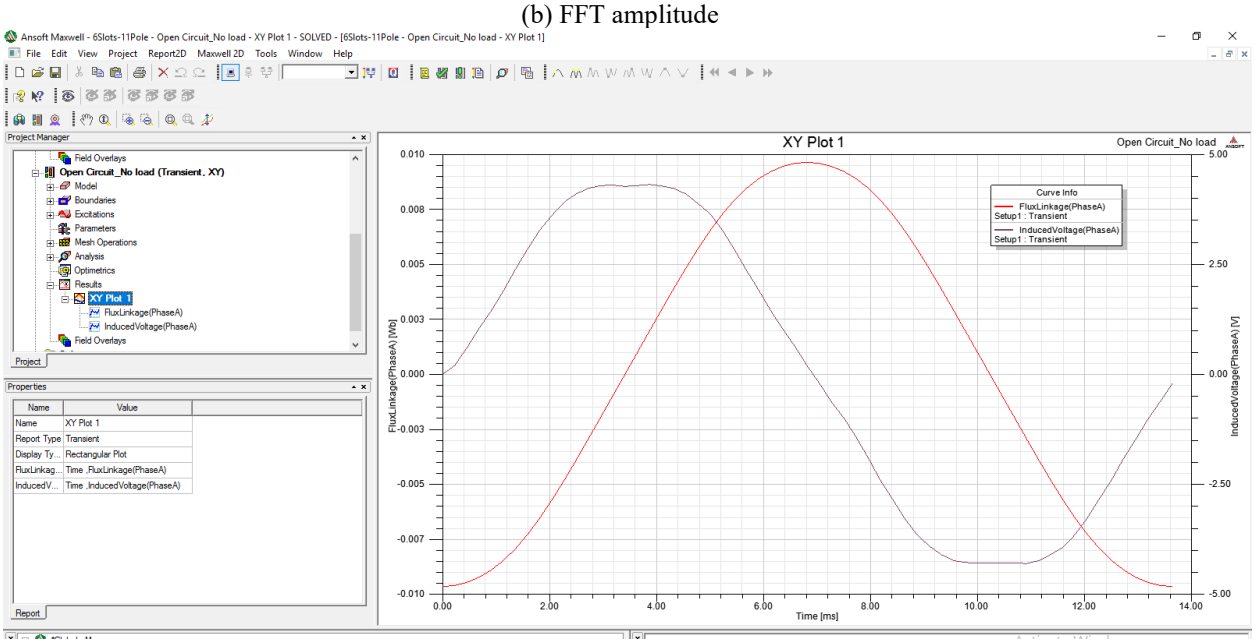

(c) FEA extracted Phase A flux linkage and EMF waveforms, 6S/11P

Fig. 4 - Comparison of electromotive force, 400 r/min

4. Load Characteristics

Large torque pulsations of the 6S/14P and 6S/10P machine types would invariably hinder its overall useable average torque value, as could be deduced from Fig. 5 (a) and (b). More so, the noticeable third (3rd) harmonic order of

the electromagnetic torque produced by 6S/10P and 6S/14P machine types is as result of the presence of even order harmonic elements of the induced voltages, as pointed out in [16]. The presence of the 3rd order harmonic component of torque would consequently lead to high torque ripple in the concerned machine types. Similarly, the visible sixth (6th) order harmonics of Fig. 5(b) is as a result of the interaction between the even-order harmonics of the induced-electromotive force and the applied sinusoidal currents. In addition, number of cycles per torque waveform is stated in Eq. 12. The number of cycles is obtained at highest value of torque harmonic element, besides the fundamental component. In this present case, 6S/10P and 6S/14P machine types would yield a value of three (3), respectively while 6S/11P and 6S/13P will result to a value of six (6) cycles. This is evident in Fig. 5. It is worth mentioning that harmonic orders of an electrical machine have different implications on various output performances such as induced voltage, torque ripple, on-load torque and no-load torque. Thus, a particular harmonic order of voltage does not have the same significance as that of its equivalent torque harmonic and vice-versa. Electromagnetic torque simulation platform of 6S/11P is shown in Fig. 5(c). Largest average torque is recorded by 6S/11P type, followed by 6S/13P machine configuration, in-line with their resulting induced-electromotive force magnitudes.

$$T_c = \frac{P_r}{GCD(P_s, P_r)} \qquad (12)$$

where: *GCD* is greatest common divisor between stator tooth number (P_s) and rotor pole number (P_r) [17].

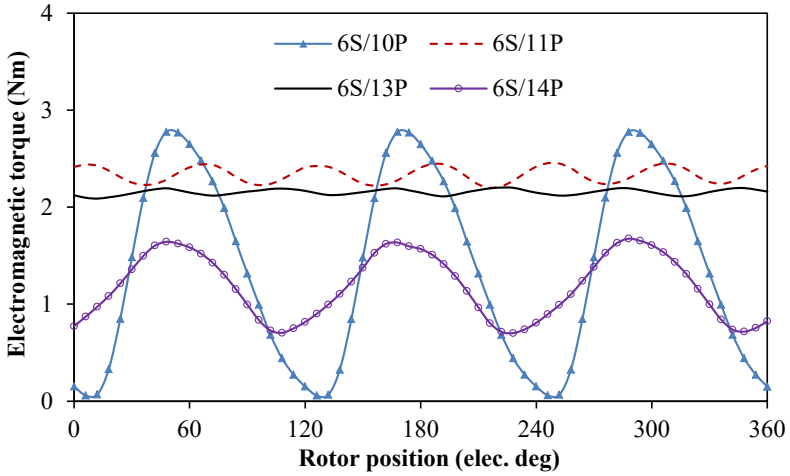

(a) Torque versus rotor position

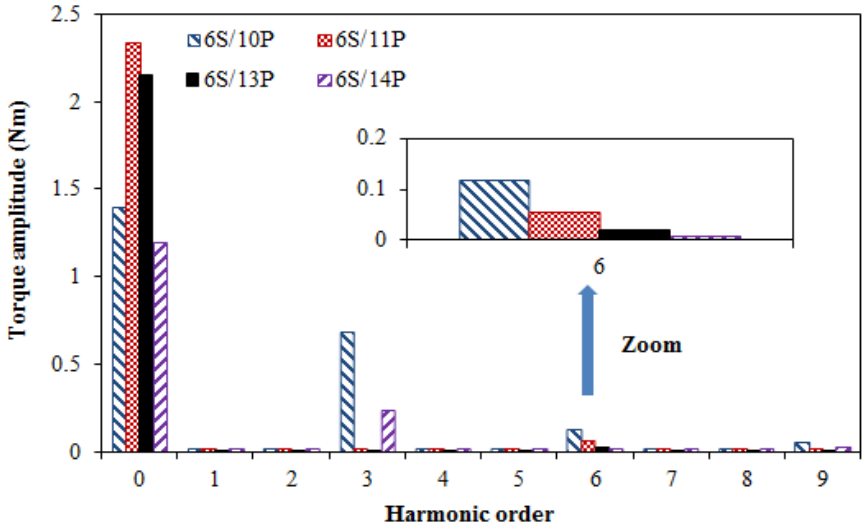

(b) FFT amplitude with a zoomed 6th order component

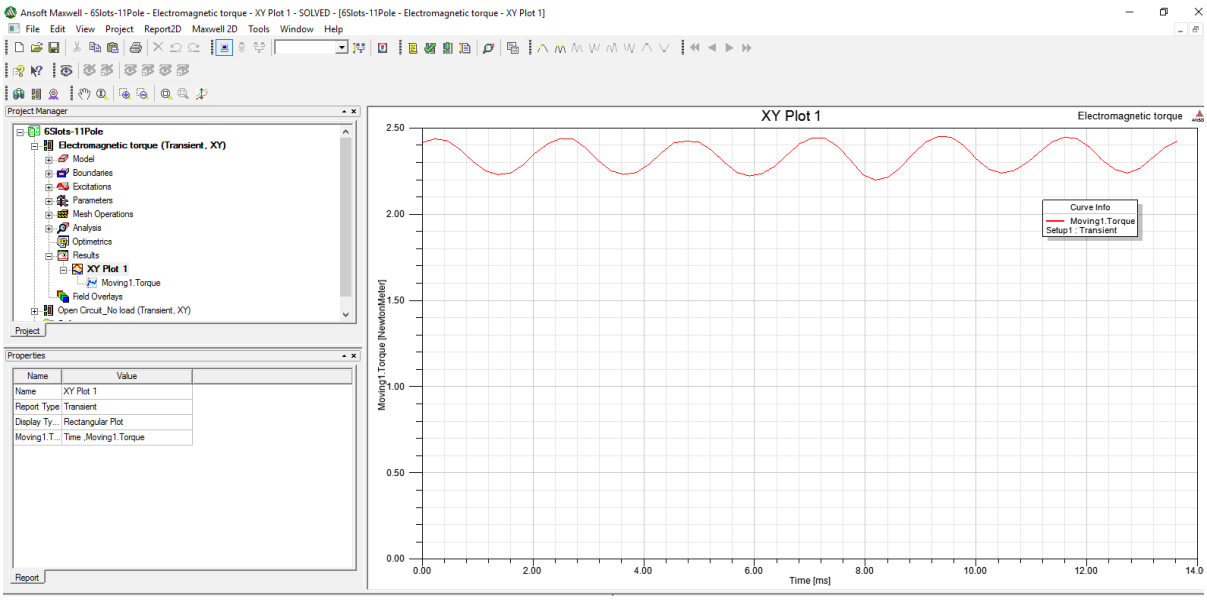

(c) FEA extracted torque waveform, 6S/11P

Fig. 5 - Comparison of electromagnetic torque at 15A

Average torque variation with applied peak load (current) and copper loss are shown in Fig. 6(a) and (b), respectively. Again, the largest average torque is obtained in the 6S/11P topology, followed by the 6S/13P machine configuration, at all the simulation conditions of electric loads. It is inferred from Fig. 6 that the machine types having $P_r=2P_s \pm 1$ would have higher ability to overcome electric overload compared to its $P_r=2P_s \pm 2$ counterparts. Also, the variation of average torque with current advance angle is presented in Fig. 6(c). It is shown that the largest average torque of the compared machine types would occur at the zero current advance angles of the machine types; though, with some slight shifts in the machine types having $P_r=2P_s \pm 2$, due its asymmetric nature.

Figs. 6(a) and (b) are predicted using the software's 2D-FEA platform through parametric analysis of the excited three-phase sinusoidal current waveforms via the software's optimetrics and sweep analysis setup section, as illustrated in Fig. 6(d) and (e). The computer-generated torque results at different current and copper loss ratings are then averaged and post processed for graphical plotting/representation. Copper loss of the investigated machine types is calculated using Eq. 13, as demonstrated in [18]. Note that the copper loss expression of the analyzed machine types is related to its other machine parameters, as given in Eq. 14. Further, current angle is predicted using the sinusoidal excitation current provided in Eq. 15.

$$P_{cu} = 3 \times I_{rms}^2 R \tag{13}$$

where: I_{rms} is root mean square value of the applied phase current, R is phase resistance.

$$R = \frac{4\rho(l + l_e)mN_{ph}^2}{Ak_pP_s} \tag{14}$$

where: ρ is l is machine stack length, l_e is end winding length, m is number of phases, N_{ph} is turns per phase, A is slot area per phase and k_p is winding factor [19].

$$I_a = \mathrm{Im}ax * \sin(Omega\_rad * Time + Thet) \tag{15}$$

where: I_a is Phase A current, *Imax* is applied peak current, Omega_rad is angular speed, *Time* is electrical period, *Thet* is current advance angle [20].

In order to create Phase A excitation winding, the following steps are taken:

1. Select the menu item, Maxwell>Excitation>Add winding
2. Insert the following in winding window: Name= PhaseA, Type= Current stranded, Current= $\mathrm{Im}ax * \sin(Omega\_rad * Time + Thet)$.

3. The process is repeated for Phase B and Phase C windings; however, with phase shift of 120° and 240°, respectively.

Note that Fig. 6(c) simulation is done over a given electric period and at varying values of *Thet* between 0° to 90°. *Thet* angular range of 0°–90° represents the angular difference between direct-axis and quadrature-axis directions of any given electrical machine. FEA extracted winding window is shown in Fig. 6(e). *Thet* is set at zero (0) degree value on predicting the average torque versus current outlines, such as in Fig. 6(a).

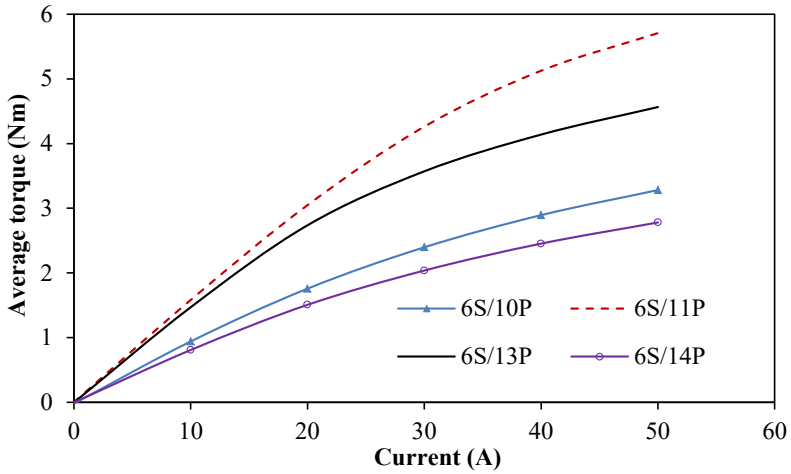

(a) Torque versus current

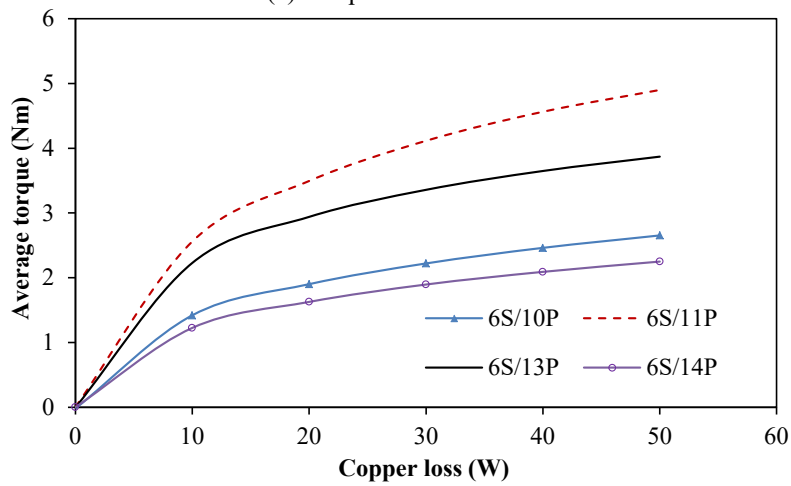

(b) Torque versus copper loss

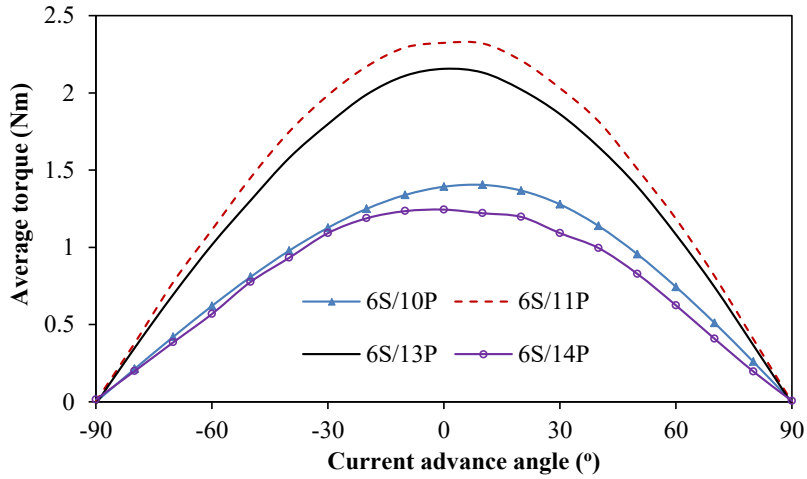

(c) Torque versus current advance angle 15A

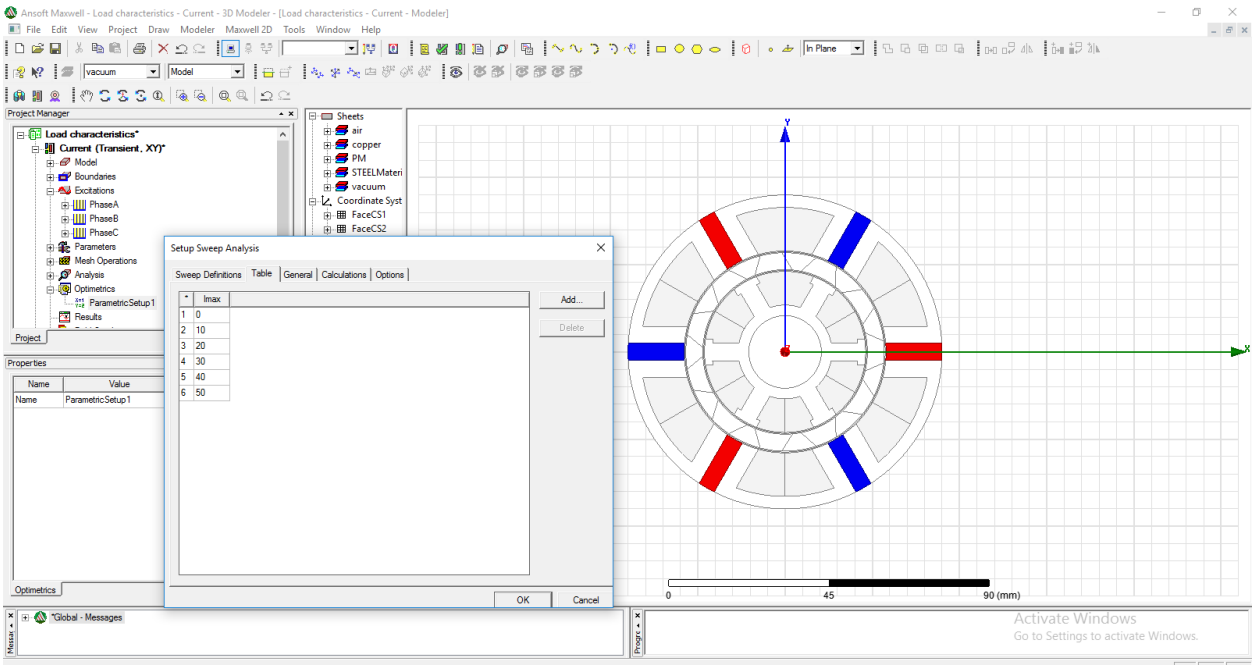

(d) Parametric settings

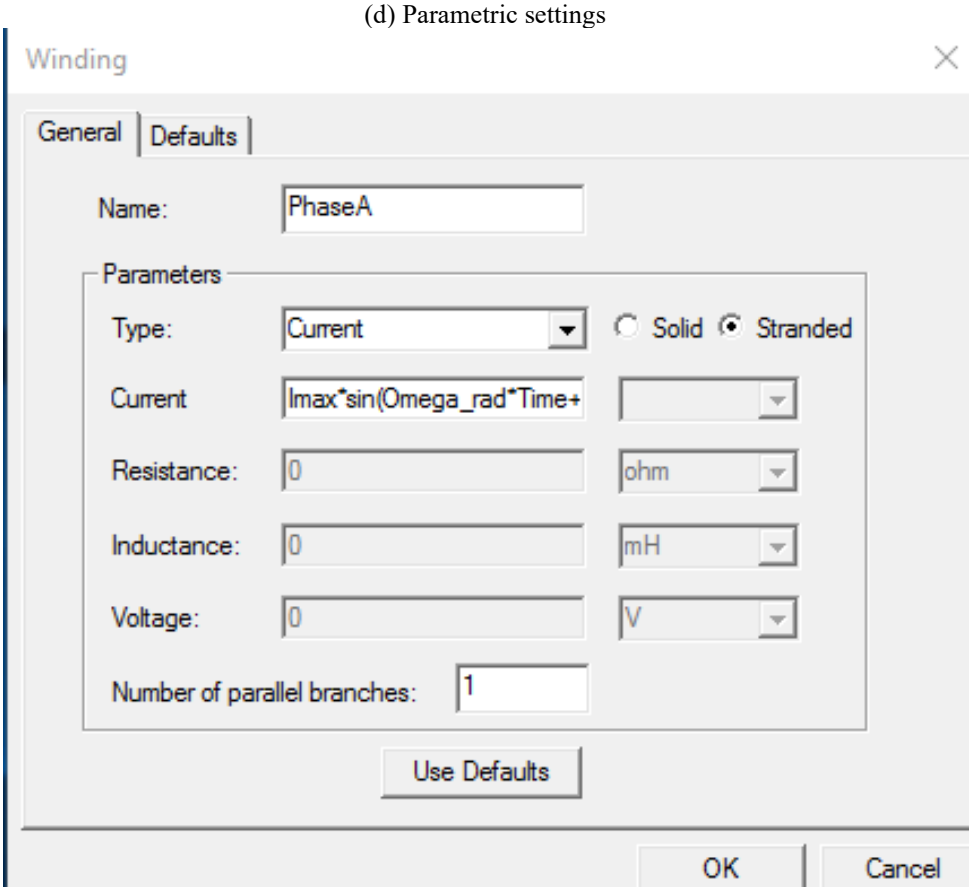

(e) Extracted winding window

Fig. 6 - Comparison of average torque at 400 r/min

Torque-speed and power-speed outlines of the compared machine models are depicted in Fig. 7(a) and (b), respectively. The obtained largest torque from the shaft is: 1.40 Nm, 2.34 Nm, 2.16 Nm and 1.27 Nm i.e. from the 6S/10P, 6S/11P, 6S/13P and 6S/14P machine types, respectively. Similarly, their corresponding maximum output power is 503.13 W, 503.05 W, 409.85 W and 394.53 W, from the 6S/10P, 6S/11P, 6S/13P and 6S/14P models, respectively. Meanwhile, the 6S/14P machine type has an excellent flux-weakening potential as shown in Fig. 7(a);

hence, it would have high ability to operate over an infinite speed range. This good flux-weakening attribute of the 6S/14P machine is wanted in traction and vehicle applications.

Fig. 8(a) shows the comparison of torque ripple in the analyzed machine types; it is obvious that the highest amount of torque ripple is recorded in the 6S/10P machine type, followed by its 6S/14P equivalent. The higher the value of torque ripples in a given electric machine, then, the higher its chances of producing noise and vibration. More so, the comparison of average torque per consumed magnet volume/material is presented in Fig. 8(b). The machine types are subjected under the same conditions of varying current densities; almost similar changing trend occurred in all the simulation scenarios. The predicted torque per applied magnet volume would invariably translate to possible cost implications of the compared machine categories. Therefore, 6S/13P machine is more promising amongst all the compared types, in terms of its economic value, since it would produce the largest torque when subjected to the same permanent magnet material usage.

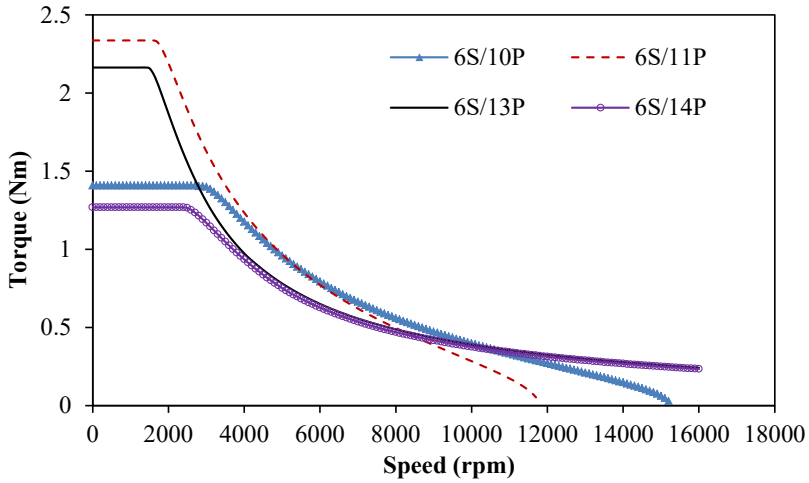

(a) Torque versus speed

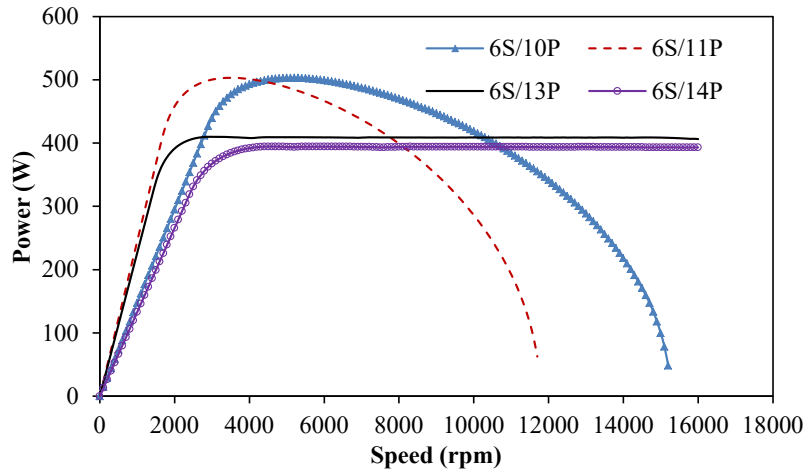

(b) Power versus speed

Fig. 7 - Comparison of torque-speed and power-speed at 15 A and 22.9 V

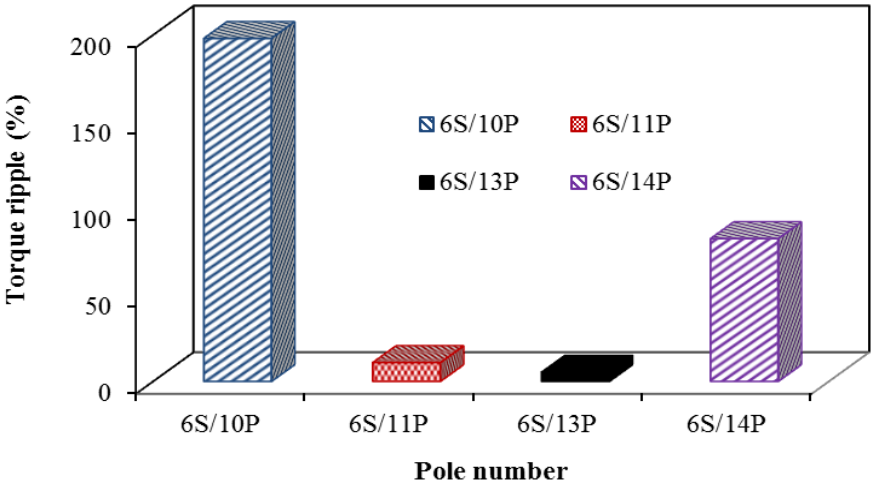

(a) Torque ripple versus pole number

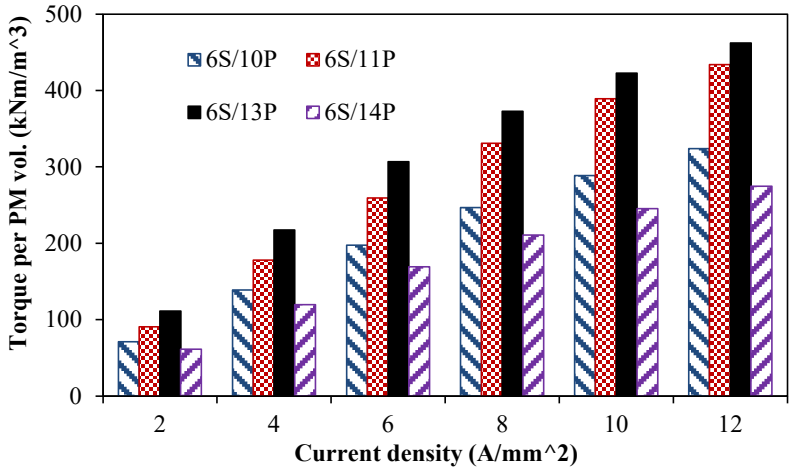

(b) Torque / magnet volume versus current density

Fig. 8 - Comparison of torque ripple and torque per magnet volume

Variation of unbalanced magnetic force in horizontal (X-axis) and vertical (Y-axis) of the rotor is presented in Fig. 9(a). It is shown that the machine types that have odd number of rotor poles, exhibit considerably larger amount of unbalanced magnetic force (UMF) on the rotor, compared to their counterparts that have even number of rotor poles. Similarly, high impact of odd number of rotor poles on the resulting UMF is reconfirmed in Fig. 9(b); negligible UMF values are obtained from 6S/10P and 6S/14P machine topologies. It is observed that the machine type having 6S/11P has the largest UMF values. Meanwhile, the results reveal that resultant force on the rotor is symmetrical over the rotor positions and insensitive to varying rotational speed, as shown in Fig. 9(c).

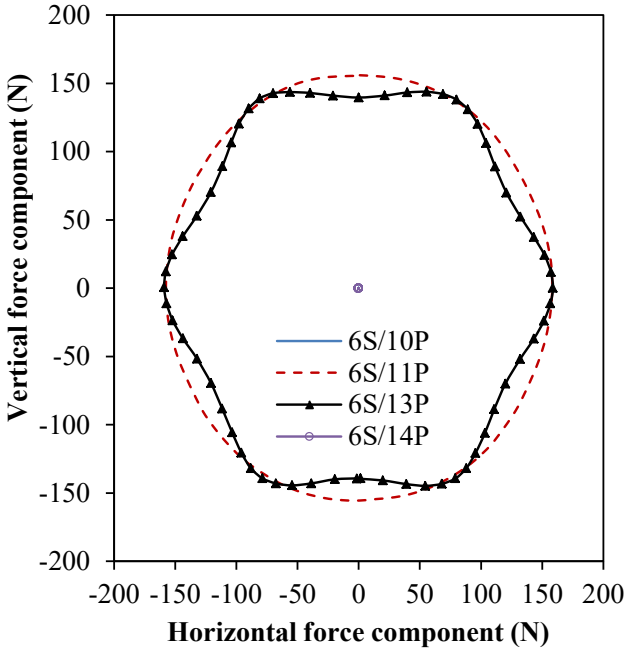

(a) Axis forces at open-circuit

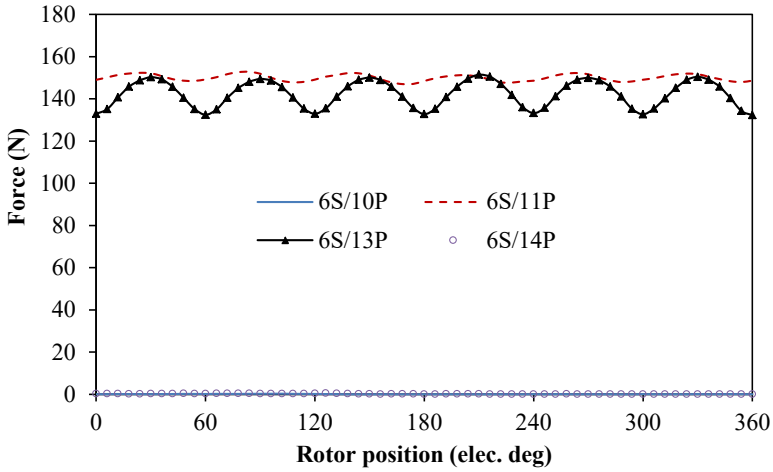

(b) UMF versus rotor position at 10 A

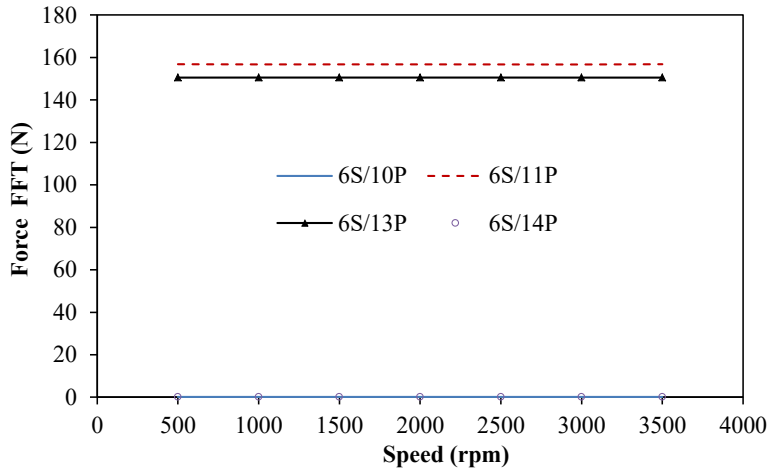

(c) UMF versus speed

Fig. 9 - Comparison of unbalanced magnetic force

Predicted friction loss (P_f) and windage loss (P_w) of the compared machine types is estimated using Eq. 16 and Eq. 17, respectively. Similarly, the core loss or iron loss of the analyzed machine types is obtained from the traditional

Bertotti loss equation given in Eq. 18. The predicted losses at rated current and speed conditions are listed in Table 2. Note that the loss coefficients are obtained from the materials' data sheet presented in [21].

$$P_f = \frac{kG\omega_m}{1000} \quad (16)$$

where: k is bearing loss coefficient (1–3), G is weight of the rotor (kg) and ω_m is shaft rotational speed (rad/s) [22].

$$P_w = 2D_{ro}^2 L_a \omega_m^3 \times 10^{-6} \quad (17)$$

where: D_{ro} is rotor diameter, L_a is machine's stack length [23].

$$P_c = K_h f B^2 + K_c f^2 B^2 + K_e f^{1.5} B^{1.5} \quad (18)$$

where: K_h, K_c and K_e is hysteresis, eddy current and excess loss coefficient, respectively [24].

Table 2 - 2D-FEA predicted loss values

Machine parameter	6S/10P	6S/11P	6S/13P	6S/14P
Friction loss, P_f (W)	0.0044	0.0035	0.0044	0.0044
Windage loss, P_w (W)	0.0153	0.0119	0.0153	0.0157
Copper loss, P_{cu} (W)	12.0825			
Phase resistance, R (Ω) at 20 °C	0.0358			
Hysteresis loss coefficient	0.0179			
Excess loss coefficient	0.0002			
Eddy current loss coefficient	2.6			
Lamination thickness (mm)	0.5			
Eddy current loss, P_e (W) at 15 A, 400 r/min	0.0848	0.0753	0.0539	0.1442
Total iron loss, P_c (W) at 15 A, 400 r/min	0.8542	0.9634	1.4029	1.3089

Computer-calculated eddy current loss due to the magnets, rotor core loss and stator core loss of the compared machines are displayed in Figs. 10(a), (b) and (c), respectively. It could be seen from Fig. 10(a) that the 6S/13P would yield the minimum amount of eddy current loss at the rated current and rated speed conditions. However, it is shown that the highest value of both the rotor and stator core losses are recorded in the 6S/13P machine type; while its corresponding lowest core losses are obtained in the 6S/10P machine topology. It is worth mentioning that the resulting value of losses in a given electrical machine would depend upon its harmonic contents, as well as on its operating frequency, which are functions of its rotor pole number and the consequent rotational speed of the rotor. Reduction of both the magnet eddy current loss and core loss in a given electrical machine could be achieved through adequate segmentation of the magnets and suitable use of soft magnetic core material, as opined in [25] and [26]. The predicted FEA total loss (including the friction and windage losses) and efficiency of the analyzed machine types are compared in Fig. 10(d).

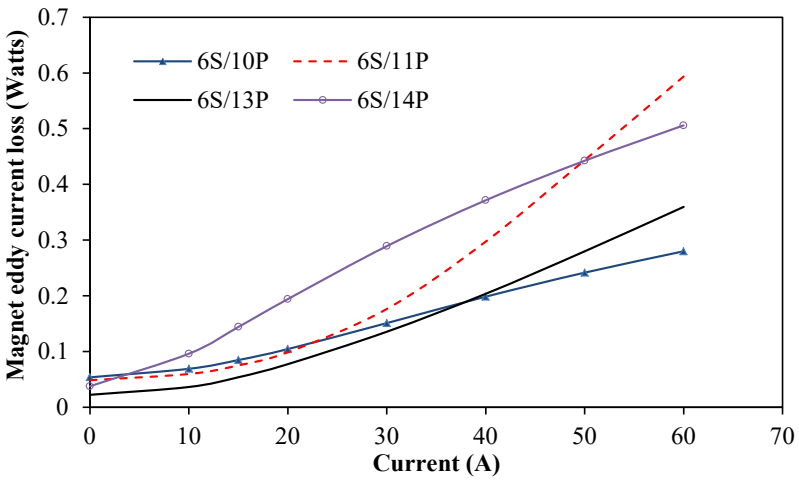

(a) Magnet eddy current loss versus load current

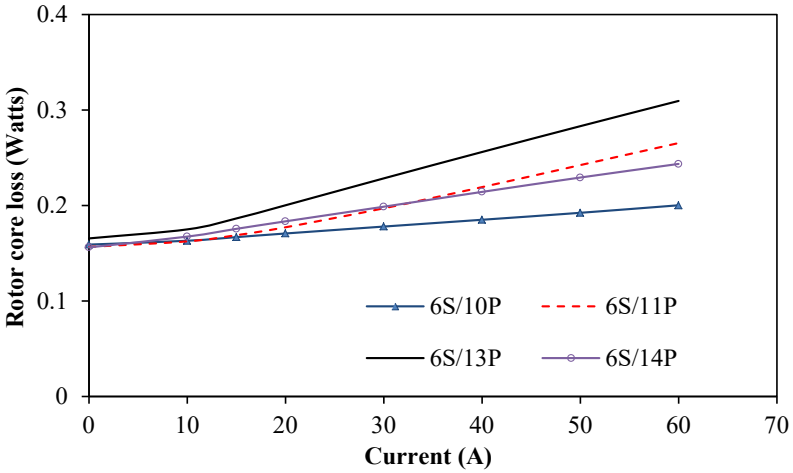

(b) Rotor core loss versus load current

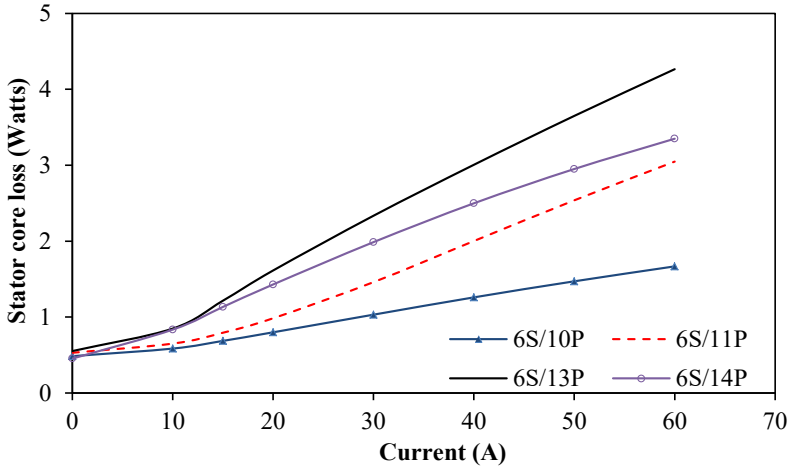

(c) Stator core loss versus load current

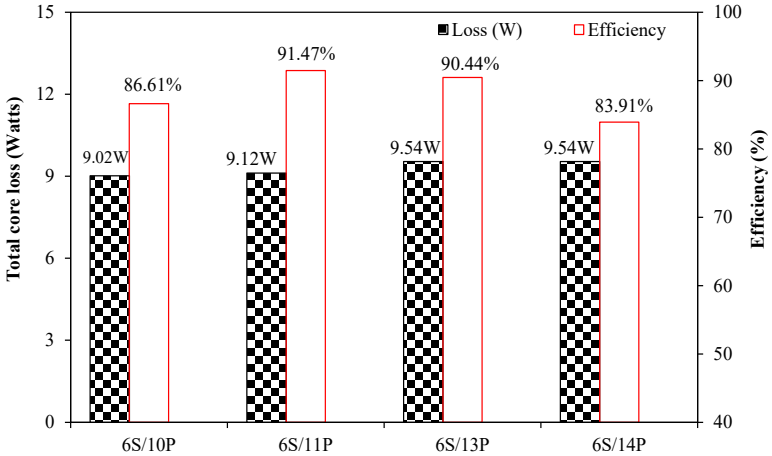

(d) Efficiency curves

Fig. 10 - Loss and efficiency comparisons, 400 r/min

Demagnetization outlines of the compared machines are depicted in Fig. 11. The demagnetization calculation is conducted under flux weakening condition and at a relatively high speed of 4000 r/min. The considered negative direct-axis currents are -15 A and -60 A. It is evident that the investigated machine types does not show any sign of partial demagnetization, and this is a commendable attribute. Nevertheless, the simulations are conducted at an ambient temperature, as provided in Table 2. It is recorded in literature that temperature and load could influence the demagnetization ability of a given permanent magnet machine [27]. The knee point of the implemented magnet material is about 0.35 T and it is ideal to investigate demagnetization characteristics of a given permanent magnet

machine within its knee point limits. Demagnetization contours of the analyzed machine show that the investigated machine has high tolerant against demagnetization effects, even at high operating speed of 4000 r/min, as shown in Fig. 11. However, in order to increase the demagnetization visual outlines of the analyzed machine types, a 0.6 T point has been adopted. It is worth noting that the applied magnets would likely respond to demagnetization influence at its deep-coloured points, as inferred from Figure 12; this demagnetization flaw would probably occur when or if the machine is operated at extreme conditions of elevated operating temperature, intense overload current and high rotor speed. It is worth mentioning that the 6S/13P machine configuration exhibits the most competitive potential against demagnetization effects, as concluded from Fig. 12 (c).

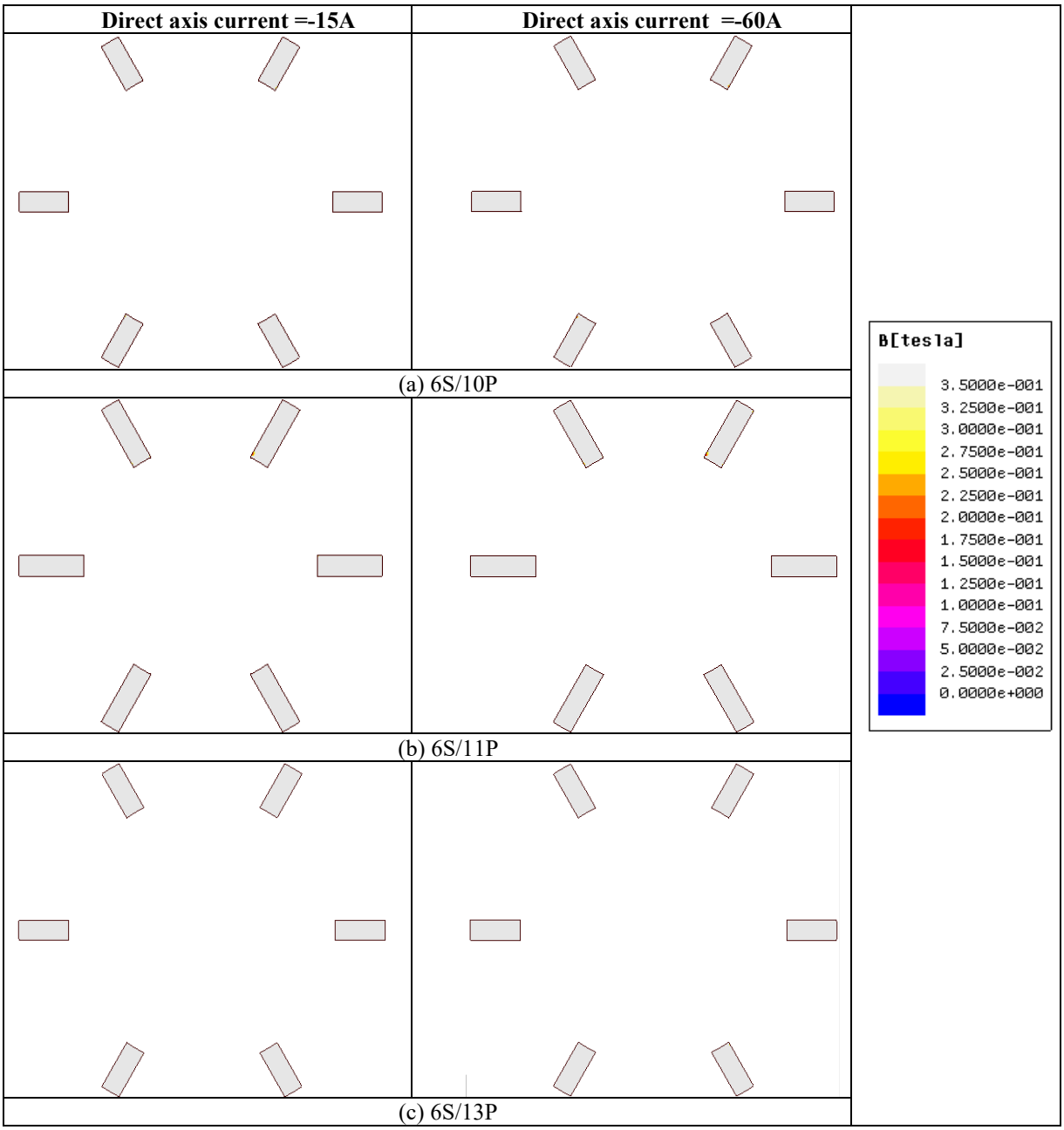

(a) 6S/10P

(b) 6S/11P

(c) 6S/13P

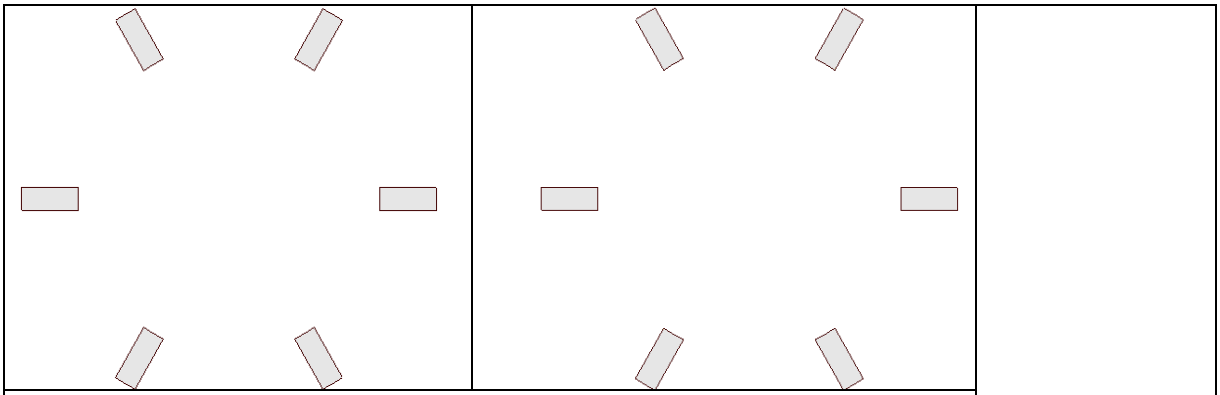

(d) 6S/14P

Fig. 11 - Demagnetization characteristics at ambient temperature, 4000 r/min at ambient temperature

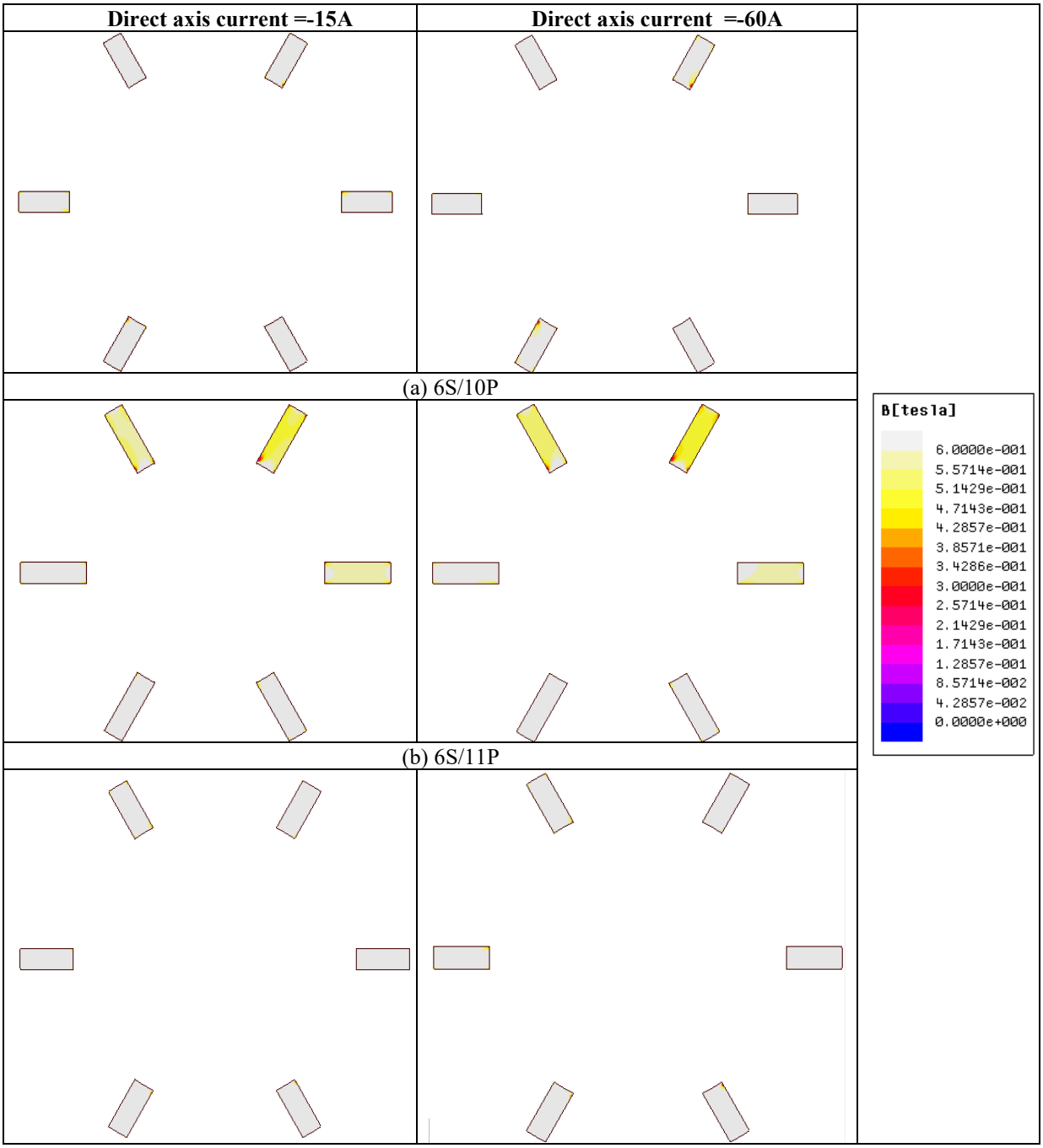

(a) 6S/10P

(b) 6S/11P

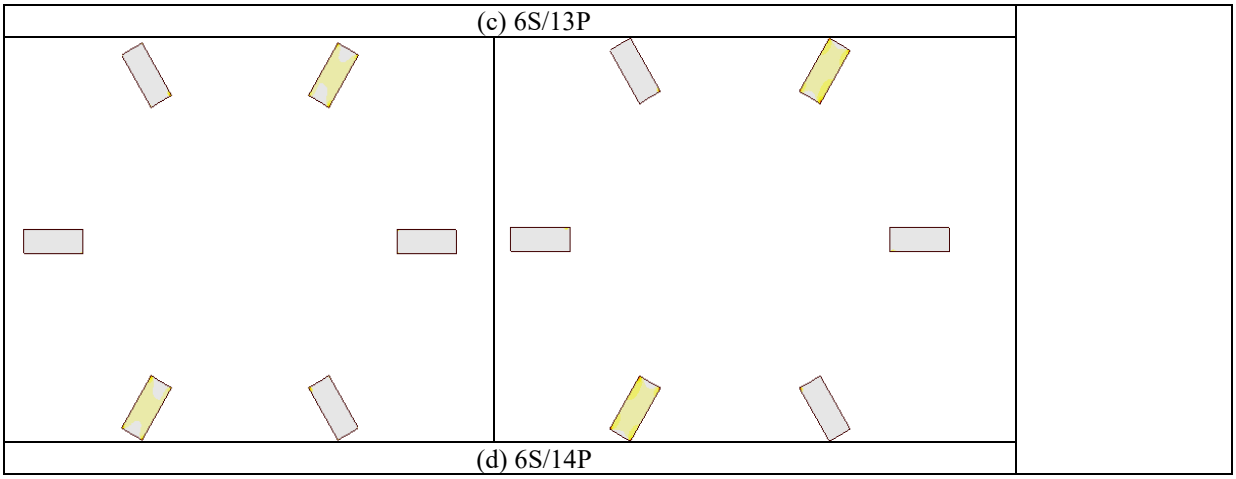

Fig. 12 - Demagnetization characteristics at ambient temperature, 4000 r/min at ambient temperature

5. Conclusion

Influence of rotor pole numbers on the output performance of a double stator flux-switching permanent magnet machine is presented. It is shown that the 6S/11P machine type has the most estimable values such as: the largest torque, EMF and flux linkage values amongst the compared machines. However, the 6S/14P machine type has the most excellent flux-weakening capability, which is looked-for in traction and vehicle applications. Nevertheless, the 6S/13P would be more economical to fabricate and commercialize, due to its ability to produce the largest torque magnitude when subjected to the same amount of permanent magnet material/volume i.e. less material usage. It is also deduced that the compared machine types have high anti-demagnetization capabilities, especially the 6S/13P configuration. More so, the analyzed machines have reasonably good efficiencies and negligible mechanical (friction and windage) loss; 6S/11P machine category has the most competitive efficiency amongst all. The compared machines would be most suitable for low-speed high-torque direct-drive uses.

Acknowledgement

The first author wishes to thank the Commonwealth Scholarship Commission, UK, for Sponsorship to run a Ph.D. Programme at the University of Sheffield, UK; during which period, this study was imagined.

References

[1] Z. Song, C. Liu and H. Zhao, "Quantitative comparison of distinct dual-stator permanent magnet vernier machines for direct-drive applications," IEEE Trans. Magn., vol. 55, no. 7, pp. 1–6, 2019.

[2] T. Zou, D. Li, R. Qu and D. Jiang, "Performance comparison of surface and spoke-type flux-modulation machines with different pole ratios," IEEE Trans. Magn., vol. 53, no. 6, pp. 1–5, 2017.

[3] M. Cheng, P. Han, Y. Du, H. Wen and X. Li, "A tutorial on general air-gap field modulation theory for electrical machines," IEEE Journal of Emerging and Selected Topics in Power Electron., vol. 10, no. 2, pp. 1712–1732, 2022.

[4] H. Zhang, W. Hua and G. Zhang, "Analysis of back-EMF waveform of a novel outer-rotor-permanent-magnet flux-switching machine," IEEE Trans. Magn., vol. 53, no. 6, pp. 1–4, 2017.

[5] L. Wu, G. Ming, L. Zhang, Y. Fang, T. Li and W. Zheng, "Comparative study between doubly salient PM machine with new stator/rotor-pole number combination and biased flux PM machine," IEEE Trans. Ind. Appl., vol. 57, no. 3, pp. 2354–2365, 2021.

[6] X. Zhu and W. Hua, "Stator-slot/rotor-pole pair combinations of flux-reversal permanent magnet machine," IEEE Trans. Ind. Electron., vol. 66, no. 3, pp. 6799–6810, 2019.

[7] P. Su, W. Hua, M. Hu, Z. Wu, J. Si, Z. Chen and M. Cheng, "Analysis of stator slots and rotor pole pairs combinations of rotor-permanent magnet flux- switching machines," IEEE Trans. on Ind. Electron., vol. 67, no. 2, pp. 906–918, 2020.

[8] C.C. Awah and Z.Q. Zhu, "Influence of rotor pole number on electromagnetic performance of double-stator Switched Flux PM Machines," In: Proceedings of the 13th IEEE Vehicle Power and Propulsion Conference (VPPC2016), Hangzhou, China, pp. 1–6, 2016.

[9] J.T. Chen, Z.Q. Zhu, "Winding configurations and optimal stator and rotor pole combination of flux-switching PM brushless AC machines," IEEE Trans. Energy Convers., vol. 25, no. 2, pp. 293–302, 2010.

[10] Z.Q. Zhu, M.L.M. Jamil and L.J. Wu, "Influence of slot and pole number combinations on unbalanced magnetic force in PM machines with diametrically asymmetric windings," IEEE Trans. Ind. Appl., vol. 49, no. 1, pp. 19–30, 2013.
[11] M.M. Reza and R.K. Srivastava, "Cogging reduction in permanent magnet machines via skewed slot opening and its analytical modeling," Progress in Electromagn. Research M, vol. 70, no. 8, pp. 167–176, 2018.
[12] H.S. Zhang, Z.X. Deng, M.L. Yang, Y. Zhang, J.Y. Tuo and J. Xu, "Analytical prediction of Halbach array permanent magnet machines considering finite tooth permeability," IEEE Trans. Magn. vol. 56, no. 6, pp. 1–10, 2020.
[13] W. Zhao, M. Cheng, W. Hua, H. Jia and R. Cao, "Back-EMF harmonic analysis and fault-tolerant control of flux-switching permanent-magnet machine with redundancy," IEEE Trans. on Ind. Electron., vol. 58, no. 5, pp. 1926–1935, 2011.
[14] W. Hua, M. Cheng, Z.Q. Zhu and D. Howe, "Analysis and optimization of back EMF waveform of a flux-switching permanent magnet motor," IEEE Trans. Energy Convers., vol. 23, no. 3, pp. 727–733, 2008.
[15] X. Xue, W. Zhao, J. Zhu, G. Liu, X. Zhu and M. Cheng, "Design of five-phase modular flux-switching permanent-magnet machines for high reliability applications," IEEE Trans. Magn., vol. 49, no. 7, pp. 3941–3944, 2013.
[16] J. Li, K. Wang, F. Li, S.S. Zhu and C. Liu, "Elimination of even-order harmonics and unipolar leakage flux in consequent-pole PM machines by employing N-S-Iron–S-N-iron rotor. IEEE Trans. Ind. Electron., vol. 66, no. 3, pp. 1736–1747, 2019.
[17] C.C. Awah, S.E. Oti and I.K. Nnabuenyi, "Pole number effects on the output of a double stator machine having magnets on the inner stator," Russian Electrical Engineering, vol. 94, no. 8, pp. 612–620, 2023.
[18] C.C. Awah, "Magnetic materials' impact on loss and efficiency profiles of dual stator permanent magnet machine," In: Proceedings IEEE Nigeria 4th International Conference on Disruptive Technologies for Sustainable Development (NIGERCON), Abuja, Nigeria, pp. 1–5, 2022.
[19] D.J. Evans and Z.Q. Zhu, "Novel partitioned stator switched flux permanent magnet machines," IEEE Trans. Magn., vol. 51, no. 1, pp. 1–14, 2015.
[20] Ansys Inc. Maxwell 2D software version 15 User's Guide, 2012, USA.
[21] A.S. Thomas, Z.Q. Zhu, G.J. Li, "Thermal modelling of switched flux permanent magnet machines," In: Proceedings of IEEE International Conference on Electrical Machines (ICEM), Berlin, Germany, pp. 2212–2217, 2014.
[22] W. Jiang, S. Feng, Z. Zhang, J. Zhang and Z. Zhang, "Study of efficiency characteristics of interior permanent magnet synchronous motors," IEEE Trans. Magn. vol. 54, no. 11, pp. 1–5, 2018.
[23] J.Y. Choi, K.J. Ko and S.M. Jang, "Experimental works and power loss calculations of surface-mounted permanent magnet machines," Journal of Magn., vol.16, no. 1, pp. 64–70, 2011.
[24] Q. Zhao and X. Liu, "Analysis of mechanical flux-weakening by using the end-cap of the switched flux permanent magnet machines," The International Journal for Computation and Mathematics in Electr. and Electrn. Eng., vol. 42, no. 2, pp. 250–260, 2023.
[25] H. Won, Y.K. Hong, M. Choi, J. Platt, B. Bryant, S. Choi, S. Li, H.S. Yoon, T.A. Haskew, J. Lee, T. Lee and T.W. Lim, "Novel design of six-phase spoke-type ferrite permanent magnet motor for electric truck application," Energies., vol. 15, no. 6, pp. 1997, 2022.
[26] U. Jamolov and G. Maizza, "Integral methodology for the multiphysics design of an automotive eddy current damper," Energies, vol. 15, no. 3, pp. 1147, 2022.
[27] Z. Jiang, X. Huang and W. Cao, "RLS-based algorithm for detecting partial demagnetization under both stationary and nonstationary conditions," Energies, vol. 15, no. 10, pp. 3509, 2022.